Cheng *et al. Energy Mater.* **2025**, *5*, 500081
**DOI:** 10.20517/energymater.2024.293

**Energy Materials**

**Article**

**Open Access**

Check for updates

# Constructing neural-like network channels from the surface to interface for enhanced high-rate cycling stability in Co-free Li-rich cathode

**Yan Cheng[1], Cheng Yang[1], Yuezhen Wang[1], Qilin Tong[1], Yunchen Ge[1], Jiang Zhu[1], Yunshan Jiang[2], Gang Sun[2], Bingbing Tian[3,*], Zhenbo Wang[2,*], Zhaozhe Yu[1,*]**

[1]Guangxi Key Laboratory of Manufacturing Systems and Advanced Manufacturing Technology, Guilin University of Electronic Technology, Guilin 541004, Guangxi, China.
[2]Shenzhen Key Laboratory of Special Functional Materials, Shenzhen Engineering Laboratory for Advanced Technology of Ceramics, Guangdong Research Center for Interfacial Engineering of Functional Materials, Guangdong Provincial Key Laboratory of New Energy Materials Service Safety, College of Materials Science and Engineering, Shenzhen University, Shenzhen 518071, Guangdong, China.
[3]International Collaborative Laboratory of 2D Materials for Optoelectronics Science and Technology of Ministry of Education, Institute of Microscale Optoelectronics, Shenzhen University, Shenzhen 518060, Guangdong, China.

***Correspondence to:** Prof. Bingbing Tian, International Collaborative Laboratory of 2D Materials for Optoelectronics Science and Technology of Ministry of Education, Institute of Microscale Optoelectronics, Shenzhen University, No. 3688, Nanhai Avenue, Yuehai Street, Nanshan District, Shenzhen 518060, Guangdong, China. E-mail: tianbb2011@szu.edu.cn; Prof. Zhenbo Wang, Shenzhen Key Laboratory of Special Functional Materials, Shenzhen Engineering Laboratory for Advanced Technology of Ceramics, Guangdong Research Center for Interfacial Engineering of Functional Materials, Guangdong Provincial Key Laboratory of New Energy Materials Service Safety, College of Materials Science and Engineering, Shenzhen University, No. 1066, Academy Avenue, Nanshan District, Shenzhen 518071, Guangdong, China. E-mail: wangzhb@hit.edu.cn; Prof. Zhaozhe Yu, Guangxi Key Laboratory of Manufacturing Systems and Advanced Manufacturing Technology, Guilin University of Electronic Technology, No. 1, Jinji Road, Dongjiang Street, Qixing District, Guilin 541004, Guangxi, China. E-mail: yuzhaozhe@guet.edu.cn

**How to cite this article:** Cheng, Y.; Yang, C.; Wang, Y.; Tong, Q.; Ge, Y.; Zhu, J.; Jiang, Y.; Sun, G.; Tian, B.; Wang, Z.; Yu, Z. Constructing neural-like network channels from the surface to interface for enhanced high-rate cycling stability in Co-free Li-rich cathode. *Energy Mater.* **2025**, *5*, 500081. https://dx.doi.org/10.20517/energymater.2024.293

**Received:** 19 Dec 2024 **First Decision:** 25 Feb 2025 **Revised:** 11 Mar 2025 **Accepted:** 25 Mar 2025 **Published:** 8 Apr 2025

**Academic Editor:** Yun Zhang **Copy Editor:** Fangling Lan **Production Editor:** Fangling Lan

## Abstract

Co-free Li-rich Mn-based cathode materials (LMNO) have gradually become powerful competitors with ultra-high specific discharge capacity and energy density. However, high-rate performance and severe voltage decay restrict the commercial application of LMNO. Herein, $LiAl_5O_8$ acts as a templating agent to construct 3D neural-like networks in LMNO, enabling fast ion diffusion and improving rate performance. Proton exchange is predominantly facilitated by the process of $LiAl_5O_8$ constructed to generate vacancies for oxygen preservation, while strong Al-O

bonds stabilize interfacial lattice oxygen, effectively suppressing voltage decay due to structural evolution. As a result, the designed cathode exhibits a discharge specific capacity of 154.65 mAh $g^{-1}$ at 5 C and 91.68% capacity retention after 400 cycles (*vs.* 66.67% of LMNO), effectively suppressing voltage decay with 90.90% voltage retention (*vs.* 81.08% of LMNO). The constructed neural-like network structure engineering provides an innovative direction for improving the high-rate performance and structural stability of LMNO.

**Keywords:** Neural-like networks, $LiAl_5O_8$, strong Al-O bonds, rate performance, Co-free Li-rich Mn-based cathode

## INTRODUCTION

The rapid development of power vehicles has put forward high requirements for energy density, security and production cost of lithium-ion batteries (LIBs)[1-4]. Therefore, it is critical to explore higher energy density cathode materials[5-8]. Among the cathode materials for LIBs, Li-rich Mn-based oxide cathodes (LLOs), $xLi_2MnO_3 \cdot (1-x)LiTMO_2$ ($0 < x < 1$, TM = Mn, Ni, Co, *etc.*), have received extensive attention because of their high specific capacity, low cost and high voltage[9-11]. Nevertheless, structural instability by transition metal migration and irreversible oxygen release of LLOs during charging/discharging cycles, particularly poor rate performance, results in impeding its practical application[12-14]. These problems can be explained by mechanisms that have been experimentally demonstrated. Firstly, the redox of oxygen and more interfacial side reactions at high voltages cause excessive consumption of Li[15-17]. Secondly, continuous oxygen release and structure collapse in LLOs lead to performance degradation, particularly the characteristic voltage fading[18-20]. Eventually, the inherent limitation of $Li^+$ migration kinetics in LLOs is the primary reason for their inability to meet rate performance requirements[21,22]. Therefore, it is imperative to conquer these challenges and upgrade the performance of LLOs to meet the high-performance requirements of power vehicles and enhance the overall performance.

To tackle the aforementioned challenges, various strategies have been explored, such as inactive element doping[23-26], structural induction[27-29], and surface engineering[30-32]. However, the effectiveness of doping alone is often limited, as it overlooks material surface side reactions that can hinder achieving higher cycle stability. Consequently, many researchers are inclined towards structural induction or surface engineering techniques to enhance the performance of LLOs. For instance, Yang *et al.* developed twin structures with a 3D $Li^+$ diffusion channel, which not only improves the rate performance but also effectively suppresses the migration of manganese ions and voltage decay[16]. The downside is that the potential instability of twins resulting from internal stress anisotropy is not taken into consideration[16]. Zheng *et al.* utilized $Li^+/Ni^{2+}$ antisite defects and surface-induced spinel phases in LLOs to enhance $Li^+$ diffusion on the surface and reduce the formation energy of oxygen vacancies, ultimately improving the rate performance and lattice oxygen stability[33]. Nevertheless, it is not enough to focus only on one-sided ion diffusion. Due to synergistic lithium-ion diffusion on the surface/bulk and structural stability, predominantly driven by subtle structural inductions and surface engineering, mainly contributes to the rate performance and overall stability of LLOs. It is well known that $LiAl_5O_8$ is an inverse spinel structure with stress equalization and a 3D $Li^+$ transport channel; thus, it exhibits both structural stability and a high rate of $Li^+$ diffusion[34-36]. Meanwhile, Al can alter the $Li@Mn_6$ superstructure units to heighten oxygen reversibility and reduce phase transitions during long cycling, and stronger Al-O bonds will improve lattice oxygen stability and transition metals migration barriers to suppress voltage decay[23,37,38].

Herein, we proposed an overall strategy to construct a neural-like network structure at the grain boundaries of primary particles and the surface of materials with $LiAl_5O_8$. The initial cathode [Co-free Li-rich Mn-based cathode materials (LMNO)] is immersed into $Al(NO_3)_3$ solution for ultrasound-induced osmotic reaction, and the Al in solution will react with Li in LMNO to form $LiAl_5O_8$ at high temperature. With the gradual

penetration of $LiAl_5O_8$ into the bulk of LMNO, a neural network-like structure of $LiAl_5O_8$ is formed, effectively enhancing the overall $Li^+$ diffusion rate and rate performance of LMNO. Meanwhile, the introduction of Al into the lattice forms strong Al-O bonds, which stabilizes interfacial lattice oxygen and effectively prevents voltage decay caused by structural evolution. The designed cathode LMNO-A shows a specific capacity of 281.55 mAh $g^{-1}$ at 0.1 C (1 C = 250 mA $g^{-1}$) and 154.65 mAh $g^{-1}$ at 5 C. After 400 cycles at 5 C, it demonstrates a capacity retention of 91.68% and a voltage retention of 90.90%. Moreover, the *in-situ* electrochemical impedance spectroscopy (EIS) test shows the average $Li^+$ diffusion rate of LMNO-A during the first charge/discharge is 3.10 × $10^{-16}$ $cm^2$ $s^{-1}$, which is higher than 1.22 × $10^{-16}$ $cm^2$ $s^{-1}$ of LMNO. This work provides a simple and reproducible modification strategy for improving the high-rate performance and significantly suppressing voltage degradation of the LMNO cathode.

## EXPERIMENTAL

### Materials preparation

$Mn_{0.75}Ni_{0.25}CO_3$ precursors were obtained by co-precipitation synthesis. The corresponding amounts of $MnSO_4·H_2O$ and $NiSO_4·6H_2O$ were calculated according to the chemical expressions of precursors and added to 500 mL of deionized water to obtain a 2 M solution. $Na_2CO_3$ was added to 500 mL of deionized water to obtain a 2 M solution as precipitant. $NH_3·H_2O$ was added to 300 mL of deionized water to obtain 0.2 M solution as a complexing agent. The three solutions were pumped into the continuously stirred tank reactor, and the stirring speed was controlled at 800 r $min^{-1}$ and the reaction temperature was 55 °C. The pH values of the nucleation, growth and aging stages were controlled at 7.8/8.0/8.2, respectively. The $Mn_{0.75}Ni_{0.25}CO_3$ obtained after the reaction was washed with deionized water 5 times, the solution was filtered off using a circulating water vacuum pump, and finally, the filtered precursor was dried in a vacuum drying oven at 120 °C for 12 h.

The dried precursor and $Li_2CO_3$ were mixed and fully ground according to the molar ratio of 1:1.2 (5% excess). The mixture was then placed in a muffle furnace, pre-sintered for 5 h at 500 °C, and sintered for 12 h at 900 °C, with the heating rate controlled at 3 °C $min^{-1}$. The final product, $Li_{1.2}Mn_{0.6}Ni_{0.2}O_2$, was obtained, marked as LMNO.

To modify the LMNO particles, $Al(NO_3)_3·9H_2O$ and LMNO were dissolved in deionized water at molar ratios of Al to transition metal (TM: Mn and Ni) of 3:100, 5:100, and 20:100, respectively. The mixture was then treated with ultrasonic waves for 30 min to ensure uniform dispersion. Afterward, the modified particles were washed three times with deionized water and dried in a vacuum oven at 120 °C to obtain the precursor. Finally, the precursor was annealed in a muffle furnace at 750 °C for 5 h with a heating rate of 3 °C $min^{-1}$ to obtain the final products, which were labeled as LMNO-A, LMNO-5A, and LMNO-20A.

Additional experimental details on the structural characterization and electrochemical properties of the electrode materials are shown in the Supplementary Material.

## RESULTS AND DISCUSSION

Neural-like network formed by $LiAl_5O_8$ permeation growth contributes to rapid $Li^+$ migration. LMNO-A is formed through impregnation treatment and sintering of LMNO, as shown in Figure 1A. $LiAl_5O_8$ is produced on the surface and then extends along the grain boundaries of the primary particles, gradually penetrating the interior to create protected structures that resemble a neural-like network. Specifically, $LiAl_5O_8$ is an anti-spinel structure, and the crystal structure includes Li-O octahedra, Al-O tetrahedra, and Al-O octahedra [Supplementary Figure 1][34]. Significantly, $LiAl_5O_8$ possesses a high $Li^+$ transport rate due to point defects such as vacancy Li ($V_{Li}$) and gap Li ($G_{Li}$)[39]. Density functional theory calculations (DFT) reveal

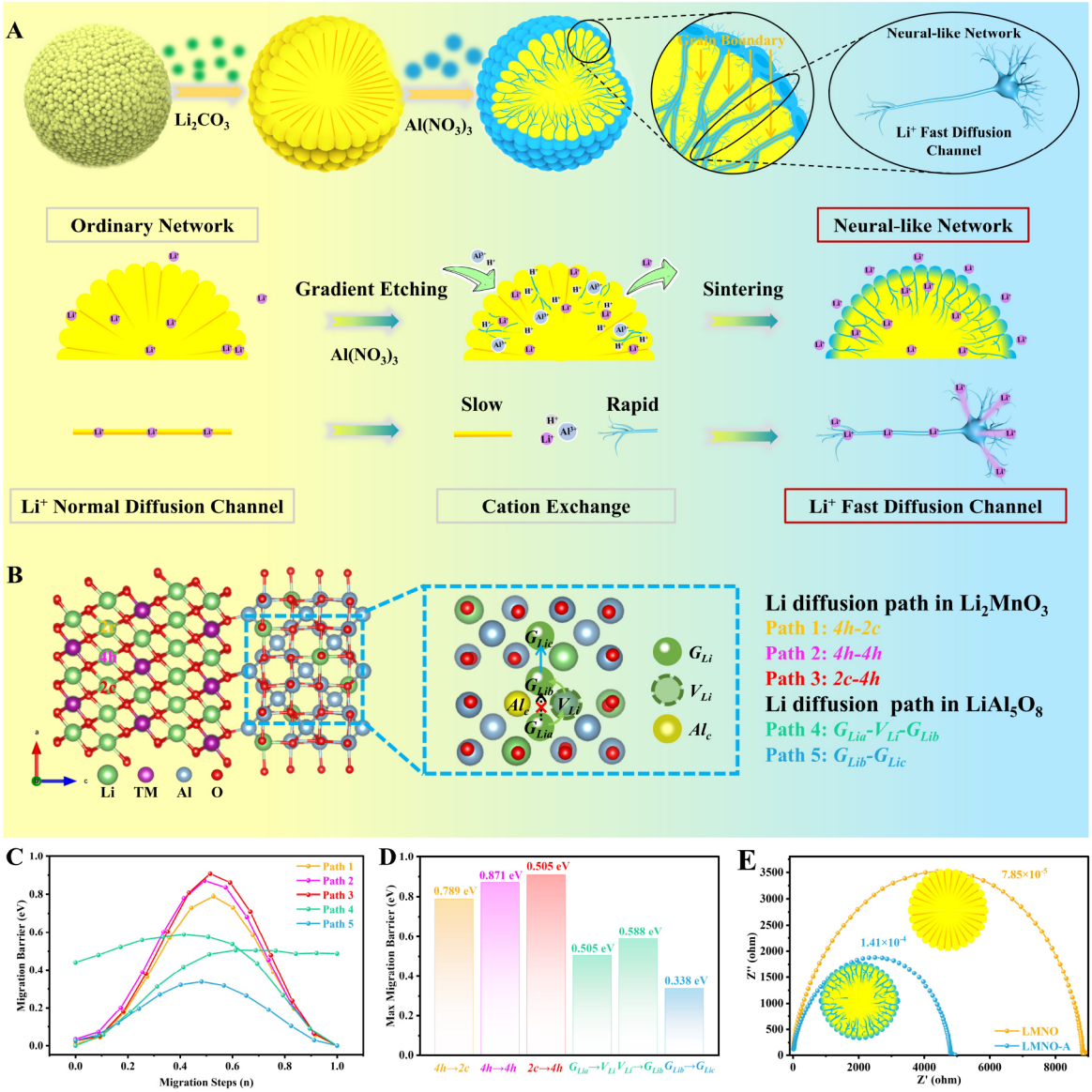


**Figure 1.** (A) The schematic of the synthesis of LMNO and LMNO-A. (B) The structural model of $LiAl_5O_8$ and $Li^+$ diffusion path in $LiAl_5O_8$. (C and D) The diffusion energy of all paths. (E) The ionic conductivity of LMNO and LMNO-A.

that $G_{Li}$ has the lowest formation energy barrier [Supplementary Table 1]. Therefore, $G_{Li}$ is used as the starting and ending point to analyze $Li^+$ migration in $LiAl_5O_8$. Additionally, the Climbing Image-Nudged Elastic Band (CI-NEB) calculations determined $Li^+$ migration paths and migration barriers [Figure 1B] that two fresh diffusion paths about $Li^+$ between two $G_{Li}$ are investigated in $LiAl_5O_8$ (Path 4 and Path 5). It is worth noting that $G_{Lia}$ cannot diffuse directly to $G_{Lib}$ due to the strong electrostatic repulsion caused by the presence of an Al atom (represented by the yellow Al atom) close to the diffusion path[34]. Instead, $G_{Lia}$ must first diffuse to $V_{Li}$ and then proceed to $G_{Lib}$. Distinguished from $LiAl_5O_8$, $Li^+$ in the $Li_2MnO_3$ phase exhibits a preference for exfoliation from the Li layer, and the exfoliation process involves three diffusion paths: Path 1, Path 2, and Path 3[40]. In a word, the corresponding diffusion energy barriers for the five diffusion paths (Path 4, Path 5, Path 1, Path 2, and Path 3) are calculated to be 0.59, 0.34, 0.79, 0.87, and 0.91 eV, respectively [Figure 1C and D]. Obviously, $Li^+$ in $LiAl_5O_8$ has a lower diffusion energy barrier and faster

diffusion rate. Furthermore, blocking electrode structures were fabricated to assess the ionic conductivity of the two samples [Figure 1E]. The results reveal that the ionic conductivity of LMNO-A is $1.41 \times 10^{-4}$ s cm$^{-1}$, significantly higher than the $7.85 \times 10^{-5}$ s cm$^{-1}$ observed for LMNO. Therefore, both theoretical calculations and preliminary experimental results confirm that the incorporation of $LiAl_5O_8$ is favorable for enhancing the $Li^+$ diffusion rate in LMNO-A.

Scanning electron microscopy (SEM) was utilized to examine the surface morphology of LMNO [Figure 2A] and LMNO-A [Figure 2B]. Both samples display typical spherical secondary particles with an approximate particle diameter of 10 μm. The primary particles of LMNO exhibit a rod-like shape and a larger diameter, growing diffusely from the center outward. In contrast, the surface of the modified LMNO-A appears relatively dense, with the primary particles becoming finer and the interior of the particles becoming porous. The observed changes in the surface morphology and particle structure of LMNO-A can be attributed to the harmonious effect of the impregnation reaction and sonication. During the impregnation reaction, the presence of $H^+$ in the acidic solution leads to the partial replacement of $Li^+$ in LMNO[41-43]. This substitution is followed by the removal of some oxygen atoms from the structure during subsequent heat treatment[31]. The elements Ni, Mn, and O are homogeneously distributed throughout the LMNO [Supplementary Figure 2]. More importantly, by analyzing the elements on the surfaces and the profile of LMNO-A, it was discovered that aluminum (Al) is not only present on the surface [Figure 2C] but also in the interior [Figure 2D] of the material. This suggests that the impregnation reaction and sonication process resulted in the incorporation of Al throughout the LMNO-A structure, rather than being limited to the surface alone. The schematic of the structure inside LMNO and LMNO-A particles is shown in Figure 2E. The pristine particles of the pristine LMNO material are loosely stacked and the grain boundaries are visible [Supplementary Figure 3]. However, the connectivity between the particles is poor, resulting in an inefficient $Li^+$ transport. In contrast, Figure 2F shows that the surface and internal structures of the modified LMNO-A samples become more compact due to the formation of neural-like $LiAl_5O_8$ channels, which fill in some of the voids between the pristine particles and optimize the grain boundary structure. Accordingly, line scanning analysis was performed to investigate the distribution of Mn, Ni, and Al in the sub-surface [Figure 2G] and interior [Figure 2H] of LMNO-A. The results indicate that Al is primarily concentrated at the grain boundaries of the primary particles in LMNO-A. Within the particles, Al is distributed similarly to its distribution in the sub-surface region. However, the relative amount of Al is lower in the bulk phases with higher Mn and Ni contents. And the line scan analysis reveals small gaps in the relative contents of all elements in different areas, as shown in Figure 2I. Under impregnation treatment and the influence of ultrasonic action, $H^+$ in the acidic solution may replace some of the $Li^+$ in LMNO particles. Due to the effect of charge balance, certain O atoms may be removed, resulting in the occurrence of cracks in primary particles. Naturally, these cracks or gaps generated may serve as pathways for Al to enter the interior of the particles, leading to differences in the distribution of Al in LMNO-A particles. Consequently, Al is primarily present in the grain boundary region of the primary particles and further penetrates the interior of the particles. Furthermore, the transmission electron microscopy (TEM) images show the existence of a structural layer on the surface of LMNO-A, which is about 3~4 nm and different from the bulk phase (Region I, Figure 2J). The layer was analyzed by Fast Fourier Transformation (FFT) and Inverse Fast Fourier Transform (IFFT) with a clear lattice streak of about 0.24 nm, which corresponds to the (311) crystal plane of the anti-spinel structure $LiAl_5O_8$ (space group: *P4-332*)[35,44,45]. Meanwhile, the bulk-phase (Region II) lattice streak of 0.47 nm corresponds to the (003) crystal plane of the *α-NaFeO*$_2$ structure (space group: *R-3m*), which is consistent with the LMNO [Supplementary Figure 4][46-48]. The X-ray diffraction (XRD) results [Supplementary Figure 5] indicate that LMNO-20A exhibits diffraction peaks at 48.8° and 66.9°, which correspond to the (330) and (440) crystal planes of $LiAl_5O_8$, respectively[44,49]. This suggests that Al reacts with part of Li in the materials, and produces $LiAl_5O_8$ after sintering at both grain boundaries of primary particles and the surface of materials. However, for the LMNO-A and LMNO-5A

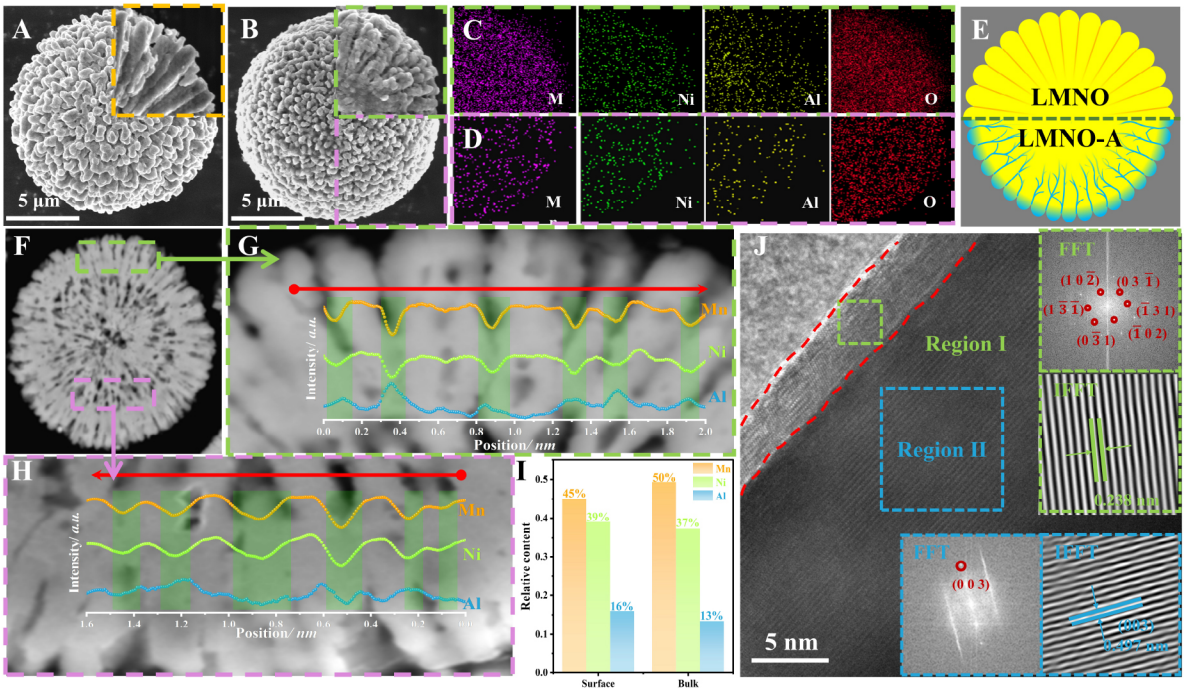


**Figure 2.** The SEM images of (A) LMNO and (B) LMNO-A. The EDS images of (C) inside and (D) surface of LMNO-A. (E) The schematic of the structure inside LMNO and LMNO-A particles. (F) The cross-section SEM images of LMNO-A. The line scan at (G) surface and (H) inside of LMNO-A and the specific relative content (I) of Mn, Ni and Al. (J) The TEM images of LMNO-A.

samples with lower $LiAl_5O_8$ content, no distinct characteristic peaks were detected due to the content being below the detection limit of XRD.

The introduction of $LiAl_5O_8$ helps to increase the oxygen vacancies in the structure and inhibit irreversible oxygen release. From the structure perspective, the crystal structures of LMNO and LMNO-A were characterized by XRD and the results are shown in Figure 3A. All the peaks belong to the hexagonal *α-NaFeO*$_2$ structure (space group: *R-3m*) and the monoclinic $Li_2MnO_3$ structure (space group: *C2/m*) for both samples[50]. In the magnified XRD patterns between 20° and 23°, the superlattice peaks of LMNO-A appear weakened compared to LMNO, which indicates a reduction in the $Li_2MnO_3$ phase content after the modification[51]. In detail, corresponding Rietveld refinements of LMNO [Figure 3B] and LMNO-A [Figure 3C] were conducted by the GSAS II program and the detailed results are shown in [Supplementary Table 2]. The fitting analysis indicates that the relative content of the $Li_2MnO_3$ phase in LMNO-A is approximately 12.80%, whereas in LMNO it is 16.40%. This variation is attributed to the replacement of $Li^+$ by $H^+$ from the hydrolysis of $Al(NO_3)_3$ in the $Li_2MnO_3$ phase, resulting in a decrease in the relative content of the $Li_2MnO_3$ phase. From the surface chemistry perspective, X-ray photoelectron spectroscopy (XPS) was carried out on LMNO and LMNO-A. Firstly, the characteristic peak can be detected at 74.2 eV in the Al 2p spectra of LMNO-A, which corresponds to $Al^{3+}$ [Figure 3D], indicating that Al is successfully introduced into the material after modification[52]. Secondly, the O 1s spectra [Figure 3E] show that the relative content of defect-oxygen in LMNO-A is boosted to 39.21% compared to that of LMNO (26.82%), which suggests an increase in the number of oxygen vacancies in the material and may be associated with a decrease in the content of the $Li_2MnO_3$ phase. Furthermore, the EPR test results [Figure 3F] further confirm the increase of oxygen vacancies, which is consistent with the analysis of the O 1s spectra[11]. Raised oxygen vacancy could contribute to inhibiting the irreversible oxygen release during the first charge/discharge process and improve the initial coulombic efficiency (ICE)[21,31]. Moreover, the relative

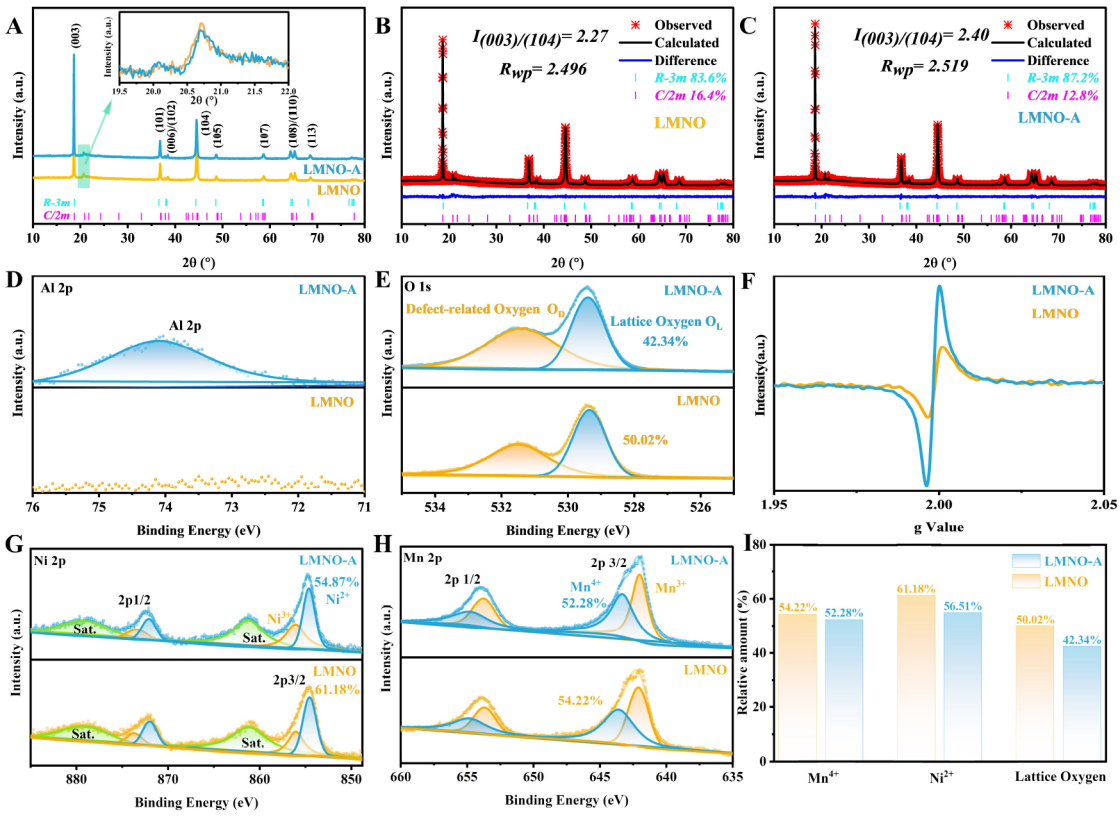


**Figure 3.** (A) The XRD patterns of LMNO and LMNO-A. The Rietveld refinement plots of (B) LMNO and (C) LMNO-A. The XPS spectra of (D) Al 2p and (E) O 1s. (F) The EPR spectrum of LMNO and LMNO-A. The XPS spectra of (G) Ni 2p and (H) Mn 2p. (I) The specific relative content of $Mn^{4+}$, $Ni^{2+}$ and lattice oxygen.

content of $Ni^{2+}$ in the corresponding Ni 2p3/2 peak at 854.5 eV is detected as 54.87% [Figure 3G]. Compared to 61.18% for LMNO, the lower $Ni^{2+}$ content is favorable for inhibiting Li/TM mixing, which is due to the similar ionic radii of $Ni^{2+}$ (0.69 A) and $Li^{+}$ (0.76 A)[25,37]. Eventually, for the Mn 2p spectra [Figure 3H], it can be found that the content of $Mn^{4+}$ in the LMNO-A samples slightly decreases (the specific value is shown in Figure 3I), which can be attributed to the decrease in the content of the $Li_2MnO_3$ phase[30,53].

In conclusion, the aforementioned results are favorable for inhibiting the irreversible release of lattice oxygen caused by the over-activation of the $Li_2MnO_3$ phase and improving the structural stability during cycling and the ICE of the electrode material.

Electrochemical properties. Assembled button half-cells with the LMNO and LMNO-A as the cathode were activated in the voltage range of 2~4.8 V at 0.1 C (1 C = 250 mA $g^{-1}$) as shown in Figure 4A. Both samples show the characteristic curve of LLO cathode materials, which included a continuous slope below 4.5 V associated with the oxidation of $Ni^{2+}/Ni^{4+}$, and a long charging plateau above 4.45 V related to the activation of the $Li_2MnO_3$ phase, where $O^{2-}$ is oxidized to $O^{(2-n)-}$ ($0 < n < 2$)[54-56]. The shorter charging plateau observed at 4.45 V in LMNO-A indicates a reduced activation of the $Li_2MnO_3$ phase. LMNO-A exhibits a reversible capacity of 281.55 mAh $g^{-1}$, compared to LMNO's reversible capacity of 268.74 mAh $g^{-1}$, with an ICE of 80.85%. The dQ/dV curves of the two samples [Figure 4B] show a significant decrease in the oxidation peak intensity of LMNO-A at around 4.5 V. This indicates that the oxygen oxidation reaction is suppressed, thereby effectively reducing irreversible oxygen release and contributing to improved structural stability and

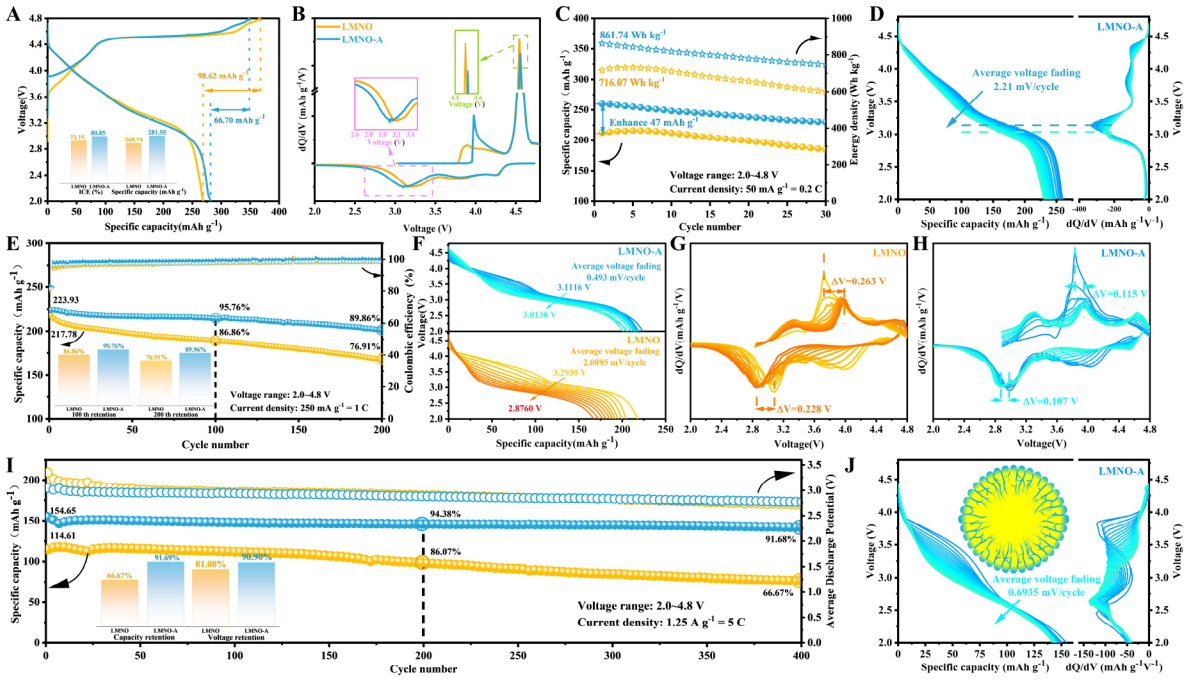


**Figure 4.** (A) The initial activation curve of LMNO and LMNO-A. (B) The dQ/dV curves of LMNO and LMNO-A. (C) The specific capacity and energy density of LMNO and LMNO-A. (D) The electrochemical behavior of LMNO-A at 0.2 C. (E) The cycling performance of LMNO and LMNO-A in the voltage range of 2~4.8 V at 1 C. (F) The Normalized discharge curves at 1 C. The corresponding dQ/dV curve of (G) LMNO and (H) LMNO-A. (I) The cycling performance of LMNO and LMNO-A in the voltage range of 2~4.8 V at 5 C. (J) The discharge curves and corresponding dQ/dV curves of 400 cycles of LMNO-A.

cycling performance of the material[40,57]. Compared to LMNO, the reduction peak potential corresponding to $Mn^{4+/3+}$ around 3.4 V is lower for LMNO-A, which can be attributed to an increased relative content of $Mn^{3+}$[57]. Moreover, LMNO-A achieves a specific capacity of 259.86 mAh $g^{-1}$ at 0.2 C and an energy density of 861.74 Wh $kg^{-1}$ [Figure 4C]. Especially, the voltage decay of LMNO-A is only 2.21 mV per cycle, whereas LNMO experiences an undesired voltage decay of up to 4.81 mV per cycle [Figure 4D and Supplementary Figure 6]. Consequently, the LMNO-A exhibits high capacity and voltage retention at 1 C, with 95.76% capacity retention after 100 cycles. Even after 200 cycles, it retains up to about 90% of its initial capacity [Figure 4E]. With severe voltage decay of 2.09 mV per cycle for LMNO, LMNO-A exhibits a surprisingly lower value of only 0.49 mV per cycle [Figure 4F]. The two pairs of redox peaks at 3.3/3.0 and 4.1/3.9 V in the dQ/dV curves at 1 C for two samples correspond to the redox processes of $Mn^{3+}/Mn^{4+}$ and $Ni^{2+}/Ni^{4+}$ in charging/discharging, respectively[25,58]. The oxidation and reduction peaks of LMNO-A [Figure 4G] around 4.0 and 3.0 V exhibited smaller polarization values of 0.12 and 0.11 V, respectively, compared to 0.26 and 0.23 V for LMNO [Figure 4H], indicating improved reversibility during cycling. Moreover, LMNO-A demonstrates an initial discharge specific capacity of 154.65 mAh $g^{-1}$ at 5 C, and after 400 cycles, it exhibits an impressive capacity retention rate of 91.68%, surpassing the specific capacity of 114.61 mAh $g^{-1}$ and retention rate of 66.67% achieved by LMNO [Figure 4I]. Significantly, after 400 cycles at 5 C, LMNO-A demonstrates a remarkable voltage retention of 90.90%, whereas LMNO only retains 81.08% of its initial voltage. Furthermore, in comparison to the voltage decay of 1.26 mV per cycle for LMNO, LMNO-A exhibits a significantly lower voltage decay of only 0.69 mV per cycle [Figure 4J and Supplementary Figure 7][25,58].

The aforementioned results indicate that the inclusion of $LiAl_5O_8$ in the system reduces interfacial side reactions, which improves the ICE and discharge specific capacity of LMNO-A. Meanwhile, the neural-like network structure constructed by $LiAl_5O_8$ on the surface extends to the interior of LMNO-A particles. It facilitates rapid diffusion of $Li^+$ inside the electrode material, thereby significantly improving the high-rate performance. Furthermore, the presence of this network structure effectively suppresses the structural evolution of the electrode, thereby inhibiting voltage decay, particularly under high-rate conditions.

The effect of neural-like network structure on the kinetics was analyzed using *in situ* EIS, Cyclic Voltammetry (CV), and Galvanostatic Intermittent Titration Technique (GITT). The EIS analysis was conducted on the two samples at various charge states within the voltage range of 2~4.8 V, using a rate of 0.2 C. The EIS data is then fitted using an equivalent circuit (refer to Supplementary Figure 8), and the specific values obtained are presented in Supplementary Table 3. The internal resistance of the solution ($R_s$) is represented by the intercept of the curve with the solid part in the high-frequency region. It is mainly related to the electronic conductivity of the cathode and the ionic conductivity of the electrolyte adsorbed on the electrode, representing the resistance of cathode electrolyte interface (CEI). The charge transfer impedance ($R_{ct}$) represents the resistance of the charge transfer process in the medium to high frequency region; the diffusion impedance of $Li^+$ ($W$) in the low frequency region represents the diffusion polarization of $Li^+$ in the electrode; $CPE_1$ indicates the capacitive components associated[18,59]. The results indicate that LMNO-A [Figure 5A] and LMNO [Figure 5B] display a similar trend of change, with minimal variation observed in the $R_s$ throughout the process. As a result, the analysis primarily focuses on examining the changes in the $R_{ct}$ and the $W$. Notably, the $R_{ct}$ exhibits almost no change from the initial stage of charging up to 3.6 V. This can be attributed to the fact that the voltage required for cation/anion oxidation has not been reached at this stage, and $Li^+$ is not yet being extracted from the cathode. On the contrary, as the charging progresses to approximately 3.8 V, the rapid extraction of $Li^+$ results in a gradual reduction of $R_{ct}$. As the charging voltage increases to 4.6 V, the oxidation of fewer lattice O atoms results in a smaller range of the $R_{ct}$ variation[25,60]. The Rct steadily rises as $Li^+$ ions are re-embedded into the cathode throughout the discharge process. Clearly, the $R_{ct}$ of LMNO remains high when discharged to 2.0 V, which may be because part of the $O^{n-}$ cannot be reduced to $O^{2-}$ or part of the $O^{2-}$ has been oxidized to $O_2$ irreversibly released. In contrast, LMNO-A exhibits significantly smaller $R_{ct}$ throughout the entire process, indicating that the modified LMNO-A possesses a more abundant lithium-ion diffusion pathway and better ionic conductivity. The diffusion impedance of $Li^+$ ($D_{Li}^+$) can be represented by the curve of $\omega^{-1/2}$ and $Z'$ [Supplementary Figure 9A and B], with the slope $\sigma$ of the curve being inversely proportional to $D_{Li}^+$. The specific $D_{Li}^+$ is calculated using the $\sigma$ values obtained from Figure 5C. The results show that LMNO-A consistently exhibits a relatively high $D_{Li}^+$ value throughout the process.

Moreover, the GITT results obtained for LMNO and LMNO-A at a rate of 0.1 C [Figure 5D and Supplementary Figure 9C] indicate that the $D_{Li}^+$ of LMNO-A consistently exceeds that of LMNO during the entire charging/discharging process lower voltage differences ($\Delta V$) and less polarization, which agreed with the previous *in-situ* EIS results. CV results [Figure 5E and Supplementary Figure 9D] showed that the peak currents and curve areas of LMNO-A were significantly larger than those of LMNO at different scan rates, indicating faster $Li^+$ deintercalation kinetics. Based on the linear relationship between the scanning speed ($v^{1/2}$) and peak current ($I_p$), we can calculate the $Li^+$ diffusion coefficients by the *Randles-Sevcik* equation[7,28]. The $D_{Li}^+$ of LMNO-A is $2.76 \times 10^{-13}$ $cm^2$ $s^{-1}$ for the charging process and $9.32 \times 10^{-14}$ $cm^2$ $s^{-1}$ for the discharging process, which is higher than those of LMNO ($2.08 \times 10^{-13}$, $6.82 \times 10^{-14}$ $cm^2$ $s^{-1}$), indicating that LMNO-A modification through $LiAl_5O_8$ significantly improves the $Li^+$ diffusion rate [Figure 5F and Supplementary Figure 9E]. The results are consistent with the *in-situ* EIS and GITT.

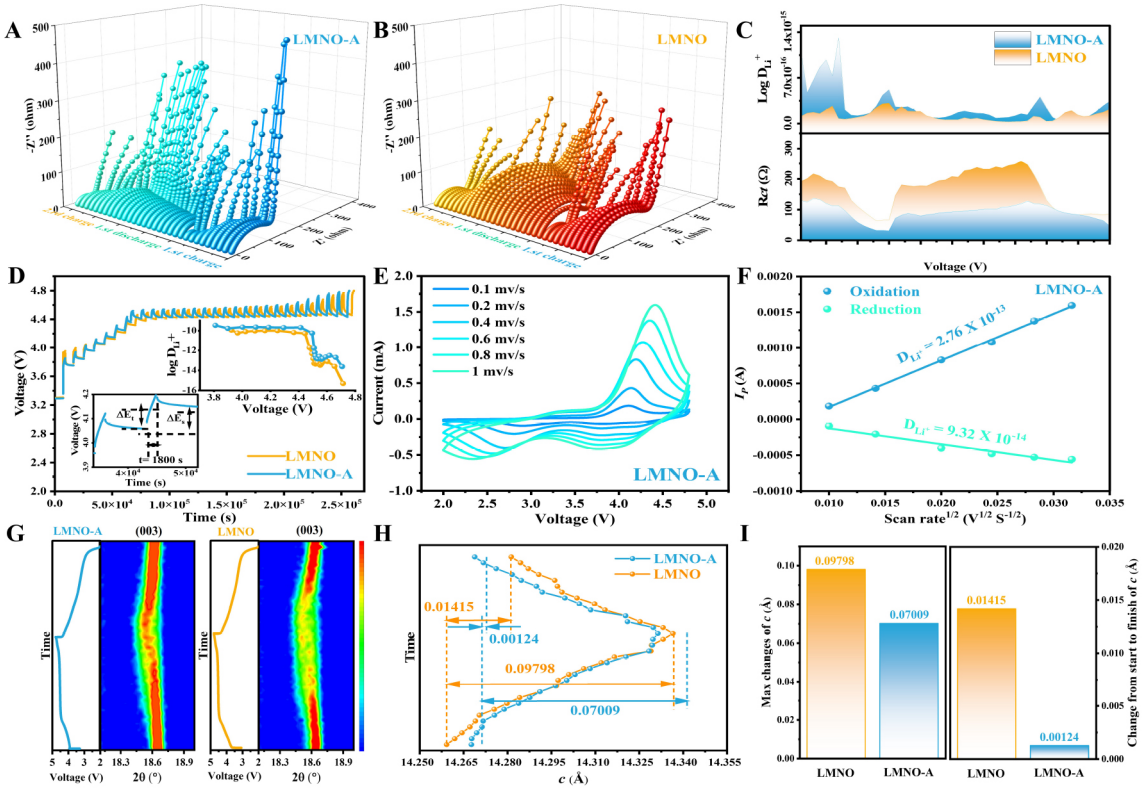


**Figure 5.** The *in-situ* EIS results of (A) LMNO-A and (B) LMNO in the first cycle and second charge. (C) The value of $D_{Li}^+$ and $R_{ct}$ of LMNO-A and LMNO in the whole process. (D)The GITT curves and the $Li^+$ diffusion coefficient of LMNO-A and LMNO. The (E) CV curves and (F) $Li^+$ diffusion coefficient for different scan rates of LMNO-A. (G)The *in situ* XRD patterns about the (003) peak of LMNO-A and LMNO during the first cycle. (H) The changes of *c* during the first cycle and (I) the corresponding parameter comparisons.

Superior initial capacity rendering and lower voltage decay during cycling are associated with a stable crystal structure. In order to explore the structural evolution during the initial charging/discharging process, *in-situ* XRD was conducted to explore the variation of the (003) and (101) peaks of LMNO-A and LMNO during initial charging/discharging [Figure 5G, Supplementary Figure 10A and B]. The results show that the two samples exhibit the same trend. During charging, $Li^+$ is consistently removed from the cathode. This can be attributed to the increased electrostatic repulsion between the neighboring oxygen layers, which leads to an expansion of the layer spacing[28]. Consequently, this expansion causes a lower-angle shift of the (003) peak during the discharging process, and the $Li^+$ is embedded back into the cathode, causing a higher-angle shift of the (003) peak as well as the (101) peak. The shifts in the positions of the (003) and (101) peaks of LMNO-A during this process are significantly smaller, which indicates better structural reversibility. However, the LMNO peak intensity is significantly lower and the full width at half maximum (FWHM) is larger at the high voltage range, which signaled a more severe decline of the layer structure[61]. We conduct a refined analysis of the *in-situ* XRD results, as shown in Figure 5H and I, Supplementary Figure 10C and D. Following the initial charging/discharging process, the changes observed in the *c*-axis and *a*-axis of LMNO-A are only $1.24 \times 10^{-3}$ and $1.45 \times 10^{-3}$ Å, respectively. In comparison, the changes in the *c*-axis and *a*-axis of LMNO are $1.42 \times 10^{-2}$ and $1.77 \times 10^{-3}$ Å, respectively. Furthermore, the maximum changes observed in the *c*-axis and *a*-axis of LMNO-A are merely $7.01 \times 10^{-2}$ and $4.97 \times 10^{-3}$ Å, while for LMNO, they are $9.8 \times 10^{-2}$ and $5.07 \times 10^{-3}$ Å. The above results suggest that the neural-like network structure facilitated by $LiAl_5O_8$ not only improves the $Li^+$ diffusion rate but also mitigates the structural evolution of LMNO-A to some extent during the charging/discharging process. Additionally, the neural-like network structure exhibits better

preservation of the layer structure, particularly at high voltages. This enhances the structural stability of the electrode during the cycling process.

To further explore the advantages of the modified material LMNO-A, we systematically compare the material characteristics after cycling. After 400 cycles at 5 C, the SEM images of the LMNO cathode reveal that most secondary particles have developed significant cracks [Figure 6A]. These cracks primarily result from stress accumulation caused by volume changes during cycling. Such structural degradation exacerbates side reactions between the cathode and the electrolyte, further accelerating material corrosion and fracture, which in turn leads to rapid capacity and voltage decay. In contrast, thanks to the presence of the $LiAl_5O_8$ neural-like network, the secondary particles of LMNO-A maintain high structural integrity under the same cycling conditions [Figure 6B]. $LiAl_5O_8$ fills the gaps between primary particles, effectively suppressing crack propagation and electrolyte corrosion, thereby endowing the material with excellent structural stability. The TEM images [Supplementary Figure 11] show that the thickness of the CEI layer on the surface of the pristine LMNO material is approximately 8 nm. This indicates that severe interfacial side reactions occur between the LMNO electrode and the electrolyte during high-rate cycling, leading to continuous thickening of the CEI layer. In contrast, for the LMNO-A material, the surface-modified $LiAl_5O_8$ layer acts as a protective barrier, effectively suppressing interfacial side reactions. As a result, the thickness of the CEI layer on LMNO-A is only 2 nm. This result demonstrates the significant role of the $LiAl_5O_8$ modification in stabilizing the interface structure and enhancing the cycling performance of the material. Moreover, the XRD tests conducted on the electrode after cycling reveal notable differences between LMNO-A and LMNO. Specifically, the intensity of the (003), (101), and (104) peaks in LMNO-A is significantly higher compared to LMNO [Figure 6C]. Additionally, the enlarged (108/110) diffraction peaks indicate a more pronounced peak splitting, reflecting better preservation of the layer structure in LMNO-A[31]. More importantly, upon disassembling the cycled battery, a notable observation is the reduced presence of black material surrounding the LMNO-A electrode. XPS tests were performed on the cycled electrodes, revealing distinct Mn characteristic signals in the Mn 2p spectra of LMNO-A. In contrast, the Mn 2p signal intensity of LMNO is significantly weaker [Supplementary Figure 12A]. To further quantify this effect, inductively coupled plasma optical emission spectroscopy (ICP-OES) was employed to measure the dissolution of Mn ions into the electrolyte for both cycled LMNO-A and LMNO electrodes. The ICP-OES results [Supplementary Figure 12B] confirm that LMNO-A exhibits significantly lower Mn dissolution compared to unmodified LMNO after 400 cycles, consistent with the XPS results. These results demonstrate that the modification not only minimizes Mn dissolution and TM migration but also significantly suppresses undesirable electrode side reactions[57]. Additionally, XPS tests conducted on the cycled electrode reveal three distinct peaks in the F 1s spectra [Figure 6D]. The presence of peaks at 684.8 eV (LiF), 686.3 eV ($Li_xPO_yF_z$), and 687.4 eV (C-F) indicates the formation of LiF and $Li_xPO_yF_z$ due to the decomposition of $LiPF_6$ in the electrolyte and the subsequent generation of HF[15]. Notably, the peak intensities of LiF and $Li_xPO_yF_z$ in LMNO-A obviously reduce compared to LMNO, suggesting a lower degree of side reactions between the cathode and the electrolyte in LMNO-A. Furthermore, the O 1s spectra [Figure 6E] show a higher relative content of TM-O in LMNO-A compared to LMNO after cycling, which suggests increased oxygen reversibility and a suppression of irreversible oxygen release in LMNO-A. Finally, the impedance characterization of the two samples after cycling using EIS [Figure 6F] reveals that the $R_{ct}$ of LMNO-A remains almost unchanged after 400 cycles, both in the fully charged and discharged states. Moreover, the $R_{ct}$ is also lower in LMNO-A compared to LMNO, indicating improved charge transfer kinetics [Figure 6G]. The $Li^+$ diffusion rate in LMNO-A is significantly higher than that in LMNO [Figure 6H]. The above test results demonstrate that the neural-like network structural strategy of simultaneous modification at internal grain boundaries and surface can improve the $Li^+$ diffusion kinetics in both spatial and temporal dimensions, inhibit the side reactions on the electrode surface, and enhance the stability of the electrode structure in the long cycling process.

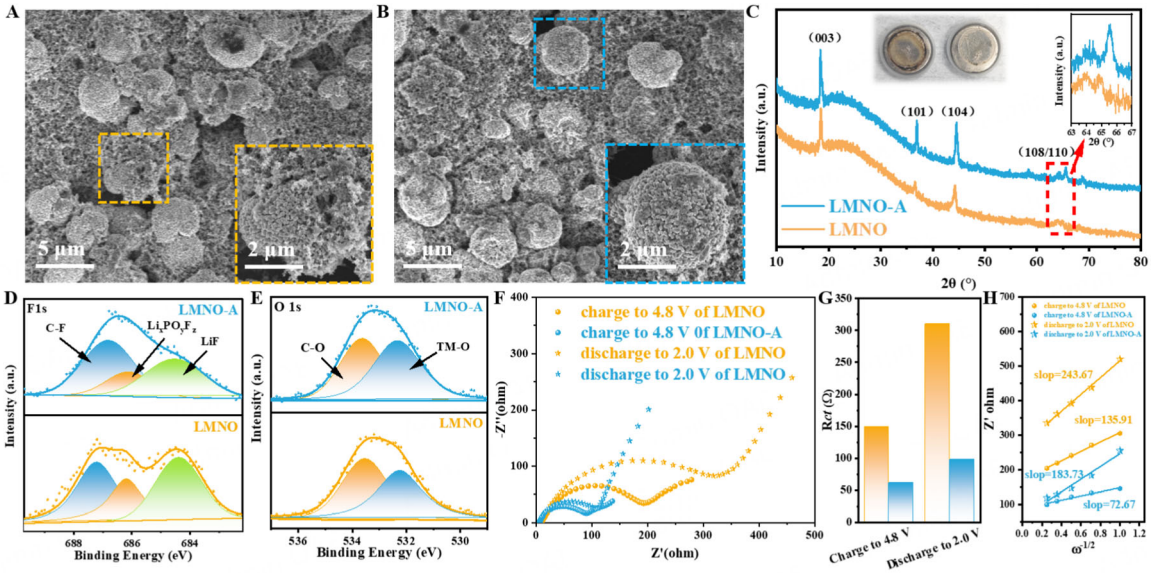


**Figure 6.** The SEM images of (A) LMNO and (B) LMNO-A after 400 cycles at 5 C. (C) The XRD patterns of LMNO and LMNO-A after cycles. The XPS spectra of (D) F 1s and (E) O 1s of LMNO and LMNO-A after cycles. The (F) EIS results of LMNO and LMNO-A after cycles at different charge states, (G) the value of $R_{ct}$ and (H) σ.

## CONCLUSIONS

In conclusion, the neural-like network structure strategy has successfully improved the electrochemical performance of Co-free Li-rich Mn-based cathodes. Different from other modification methods, the incorporation of $LiAl_5O_8$ not only covers the surface of LMNO-A particles but also gradually extends to the interior grain boundaries, forming a comprehensive neural-like network structure throughout the cathode. On the one hand, abundant 3D $Li^+$ diffusion channels are provided at the internal interfaces and surfaces from the kinetic point of view, which significantly improves the high-rate performance of the electrode materials. On the other hand, less interfacial side reactions and high lattice oxygen stability, suppress the structural evolution, significantly reduce voltage decay, and improve the structural stability of electrodes. Therefore, the designed LMNO-A cathode has excellent capacity retention/voltage retention (91.68%/90.90%) at 5 C. Currently, all-solid-state batteries require cathodes that match safer and better interfacial contact, and this strategy improves the ionic conductivity of Li-rich cathodes, providing a new way to solve the interfacial contact problem and offering new possibilities for Li-rich commercialization.

## DECLARATIONS

### Authors' contributions

Methodology and formal analysis: Cheng, Y.; Yang, C.; Wang, Y.; Tong, Q.; Ge, Y.; Zhu, J.
Writing - original draft: Yang, C.; Wang, Y.
Data analysis and technical support: Yang, C.; Wang, Y.; Tong, Q.; Ge, Y.; Zhu, J.; Jiang, Y.
Data acquisition: Yang, C.; Wang, Y.; Tong, Q.; Jiang, Y.
Supervision, writing - review and editing: Cheng, Y.; Ge, Y.; Sun, G.; Tian, B.; Wang, Z.; Yu, Z.
Resources, Project administration, Funding acquisition: Cheng, Y.; Sun, G.; Wang, Z.; Yu, Z.
Investigation: Cheng, Y.; Yang, C.; Wang, Y.; Zhu, J.; Jiang, Y.; Tian, B.; Wang, Z.; Yu, Z.

### Availability of data and materials

The data supporting our findings can be found in the Supplementary Material.

**Financial support and sponsorship**

This study was financially supported by the Guangxi Natural Science Foundation (Grant Nos. 2024GXNSFFA010002, 2023GXNSFAA026358 and 2021AB17045), Guangxi Key Laboratory of Manufacturing Systems Foundation (Grant No. 23354S008), Engineering Research Center Foundation of Electronic Information Materials and Devices (Grant No. EIMD-AA202005), the National Key Research and Development Program of China (2023YFB2406100), the National Natural Science Foundation of China (Grant Nos. 22075062 and U23A20573), Heilongjiang Touyan Team (Grant No. HITTY-20190033), and the Fundamental Research Funds for the Central Universities (Grant No. FRFCU5710051922).

**Conflicts of interest**

All authors declared that there are no conflicts of interest.

**Ethical approval and consent to participate**

Not applicable.

**Consent for publication**

Not applicable.



## REFERENCES

1. Armand, M.; Tarascon, J. M. Building better batteries. *Nature* **2008**, *451*, 652-7. DOI PubMed
2. He, W.; Zhuang, Y.; Mei, J.; et al. In situ induced lattice-matched interfacial oxygen-passivation-layer endowing Li-rich and Mn-based cathodes with ultralong life. *Small* **2022**, *18*, e2200942. DOI
3. Yang, X.; Wang, S.; Han, D.; et al. Structural origin of suppressed voltage decay in single-crystalline Li-rich layered $Li[Li_{0.2}Ni_{0.2}Mn_{0.6}]O_2$ cathodes. *Small* **2022**, *18*, e2201522. DOI
4. Yu, Z.; Lu, Q.; Wang, Y.; et al. Self-compacting engineering to achieve high-performance lithium-rich layered oxides cathode materials. *Appl. Surf. Sci.* **2023**, *619*, 156683. DOI
5. Yu, Z.; Yu, K.; Ji, F.; et al. Enhancing the cycling stability of a hollow architecture Li-rich cathode *via* Ce-integrated surface/interface/doping engineering. *Inorg. Chem. Front.* **2023**, *10*, 682-91. DOI
6. Wang, T.; Zeng, W.; Zhu, J.; et al. $SeO_2$-infused grain boundaries effectively improve rate and stability performance of Li-rich manganese-based layered cathode materials. *Nano. Energy.* **2023**, *113*, 108577. DOI
7. Xu, Z.; Guo, X.; Wang, J.; et al. Restraining the octahedron collapse in lithium and manganese rich NCM cathode toward suppressing structure transformation. *Adv. Energy. Mater.* **2022**, *12*, 2201323. DOI
8. Liang, C.; Cheng, Y.; Lv, C.; et al. Surface oxygen-locked $LiNi_{0.6}Mn_{0.4}O_2$: towards stable cycling at 4.7 V. *Energy. Storage. Mater.* **2025**, *75*, 104087. DOI
9. Assat, G.; Foix, D.; Delacourt, C.; Iadecola, A.; Dedryvère, R.; Tarascon, J. M. Fundamental interplay between anionic/cationic redox governing the kinetics and thermodynamics of lithium-rich cathodes. *Nat. Commun.* **2017**, *8*, 2219. DOI PubMed PMC
10. Sun, Z.; Xu, L.; Dong, C.; et al. A facile gaseous sulfur treatment strategy for Li-rich and Ni-rich cathode materials with high cycling and rate performance. *Nano. Energy.* **2019**, *63*, 103887. DOI
11. Hao, Y.; Li, X.; Liu, W.; et al. Interfacial Mn vacancy for Li-rich Mn-based oxide cathodes. *ACS. Appl. Mater. Interfaces.* **2022**, *14*, 22161-9. DOI
12. He, J.; Ma, H.; Zhang, H.; et al. Promoting the electrochemical performance of Li-rich layered $Li_{1.2}(Ni_{1/6}Co_{1/6}Mn_{4/6})_{0.8}O_2$ with the in situ transformed allogenic spinel phase. *ACS. Sustain. Chem. Eng.* **2020**, *8*, 2215-25. DOI
13. Yang, C.; Wang, H.; Wei, Z.; et al. One-step simultaneous construction of oxygen vacancies and Mo-O bonds to enhance the cyclic stability of lithium-rich manganese-based layered oxides. *J. Alloys. Compd.* **2025**, *1010*, 178267. DOI
14. Wang, K.; Qiu, J.; Hou, F.; et al. Unraveling the role of surficial oxygen vacancies in stabilizing Li-rich layered oxides. *Adv. Energy. Mater.* **2023**, *13*, 2301216. DOI
15. Guo, W.; Zhang, Y.; Lin, L.; et al. Enhancing cycling stability in Li-rich Mn-based cathode materials by solid-liquid-gas integrated interface engineering. *Nano. Energy.* **2022**, *97*, 107201. DOI
16. Yang, Y.; Gao, C.; Luo, T.; et al. Unlocking the potential of Li-rich Mn-based oxides for high-rate rechargeable lithium-ion batteries. *Adv. Mater.* **2023**, *35*, e2307138. DOI
17. Li, X.; Yu, F.; Ke, W.; et al. Modulating local electronic structure enhances superior electrochemical activity in Li-rich oxide cathodes.

*J. Mater. Chem. A.* **2023**, *11*, 2252-61. DOI
18. Kim, S. Y.; Park, C. S.; Hosseini, S.; Lampert, J.; Kim, Y. J.; Nazar, L. F. Inhibiting oxygen release from Li-rich, Mn-rich layered oxides at the surface with a solution processable oxygen scavenger polymer. *Adv. Energy. Mater.* **2021**, *11*, 2100552. DOI
19. Wen, X.; Yin, C.; Qiu, B.; et al. Controls of oxygen-partial pressure to accelerate the electrochemical activation in Co-free Li-rich layered oxide cathodes. *J. Power. Sources.* **2022**, *523*, 231022. DOI
20. Jiang, W.; Zhang, C.; Feng, Y.; et al. Achieving high structure and voltage stability in cobalt-free Li-rich layered oxide cathodes via selective dual-cation doping. *Energy. Storage. Mater.* **2020**, *32*, 37-45. DOI
21. Feng, Z.; Song, H.; Li, Y.; Lyu, Y.; Xiao, D.; Guo, B. Adjusting oxygen redox reaction and structural stability of Li- and Mn-rich cathodes by Zr-Ti dual-doping. *ACS. Appl. Mater. Interfaces.* **2022**, *14*, 5308-17. DOI
22. Su, Y.; Zhao, J.; Dong, J.; et al. Atomic pins bridging integrated surface to assist high-rate stability for Co-free Li-rich cathode. *Chem. Eng. J.* **2023**, *475*, 145991. DOI
23. Li, S.; Yang, L.; Liu, Z.; et al. Surface Al-doping for compromise between facilitating oxygen redox and enhancing structural stability of Li-rich layered oxide. *Energy. Storage. Mater.* **2023**, *55*, 356-63. DOI
24. Zhang, K.; Sheng, H.; Wu, X.; et al. Improving electrochemical properties by sodium doping for lithium-rich layered oxides. *ACS. Appl. Energy. Mater.* **2020**, *3*, 8953-9. DOI
25. Cheng, W.; Ding, J.; Liu, Z.; et al. Zn/Ti dual concentration-gradients surface doping to improve the stability and kinetics for Li-rich layered oxides cathode. *Chem. Eng. J.* **2023**, *451*, 138678. DOI
26. Wang, E.; Xiao, D.; Wu, T.; et al. Al/Ti synergistic doping enhanced cycle stability of Li-rich layered oxides. *Adv. Funct. Mater.* **2022**, *32*, 2201744. DOI
27. Luo, D.; Ding, X.; Fan, J.; et al. Accurate control of initial coulombic efficiency for lithium-rich manganese-based layered oxides by surface multicomponent integration. *Angew. Chem. Int. Ed.* **2020**, *59*, 23061-6. DOI
28. Tan, Z.; Li, Y.; Xi, X.; et al. A novelty strategy induced pinning effect and defect structure in Ni-rich layered cathodes towards boosting its electrochemical performance. *J. Energy. Chem.* **2022**, *72*, 570-80. DOI
29. Marie, J. J.; House, R. A.; Rees, G. J.; et al. Trapped $O_2$ and the origin of voltage fade in layered Li-rich cathodes. *Nat. Mater.* **2024**, *23*, 818-25. DOI PubMed PMC
30. Yan, C.; Shao, Q.; Yao, Z.; et al. Multifunctional surface construction for long-term cycling stability of Li-rich Mn-based layered oxide cathode for Li-ion batteries. *Small* **2022**, *18*, e2107910. DOI
31. Zhang, G.; Chen, M.; Li, C.; et al. Surface spinel and interface oxygen vacancies enhanced lithium-rich layered oxides with excellent electrochemical performances. *Chem. Eng. J.* **2022**, *443*, 136434. DOI
32. Liu, Y.; Zhu, H.; Zhu, H.; et al. Modulating the surface ligand orientation for stabilized anionic redox in Li-rich oxide cathodes. *Adv. Energy. Mater.* **2021**, *11*, 2003479. DOI
33. Zheng, H.; Zhang, C.; Zhang, Y.; et al. Manipulating the local electronic structure in Li-Rich layered cathode towards superior electrochemical performance. *Adv. Funct. Mater.* **2021**, *31*, 2100783. DOI
34. Mo, S.; Zhang, B.; Zhang, K.; Li, S.; Pan, F. $LiAl_5O_8$ as a potential coating material in lithium-ion batteries: a first principles study. *Phys. Chem. Chem. Phys.* **2019**, *21*, 13758-65. DOI
35. Wu, Y.; Lei, D.; Wang, C. The formation of $LiAl_5O_8$ nanowires from bulk Li-Al alloy enables dendrite-free Li metal batteries. *Mater. Today. Phys.* **2021**, *18*, 100395. DOI
36. Aykol, M.; Kim, S.; Hegde, V. I.; et al. High-throughput computational design of cathode coatings for Li-ion batteries. *Nat. Commun.* **2016**, *7*, 13779. DOI PubMed PMC
37. Li, Z.; Li, Y.; Zhang, M.; et al. Modifying $Li@Mn_6$ Superstructure units by Al substitution to enhance the long-cycle performance of Co-free Li-rich cathode. *Adv. Energy. Mater.* **2021**, *11*, 2101962. DOI
38. Zhang, C.; Wei, B.; Wang, M.; et al. Regulating oxygen covalent electron localization to enhance anionic redox reversibility of lithium-rich layered oxide cathodes. *Energy. Storage. Mater.* **2022**, *46*, 512-22. DOI
39. Li, Z.; Tian, F.; Li, Y.; Lei, D.; Wang, C. Zero-strain insertion anode material of lithium-ion batteries. *Small* **2022**, *18*, e2204875. DOI
40. Zhang, Y.; Zheng, S.; Meng, C.; et al. A near-surface structure reconfiguration strategy to regulate $Mn^{3+}/Mn^{4+}$and $O^{2-}/O^{2n-}$ redox for stabilizing lithium-rich oxide cathode. *Adv. Funct. Mater.* **2023**, *33*, 2300987. DOI
41. Liu, P.; Zhang, H.; He, W.; et al. Lithium deficiencies engineering in Li-rich layered oxide $Li_{1.098}Mn_{0.533}Ni_{0.113}Co_{0.138}O_2$ for high-stability cathode. *J. Am. Chem. Soc.* **2019**, *141*, 10876-82. DOI
42. Rosina, K. J.; Jiang, M.; Zeng, D.; Salager, E.; Best, A. S.; Grey, C. P. Structure of aluminum fluoride coated $Li[Li_{1/9}Ni_{1/3}Mn_{5/9}]O_2$ cathodes for secondary lithium-ion batteries. *J. Mater. Chem.* **2012**, *22*, 20602. DOI
43. Yu, R.; Banis, M. N.; Wang, C.; et al. Tailoring bulk $Li^+$ ion diffusion kinetics and surface lattice oxygen activity for high-performance lithium-rich manganese-based layered oxides. *Energy. Storage. Mater.* **2021**, *37*, 509-20. DOI
44. Singh, V.; Chakradhar, R.; Rao, J.; Kwak, H. Characterization, EPR and photoluminescence studies of $LiAl_5O_8$:Cr phosphors. *Solid. State. Sci.* **2009**, *11*, 870-4. DOI
45. Singh, V.; Chakradhar, R.; Rao, J.; Kim, D. EPR and luminescence properties of combustion synthesized $LiAl_5O_8$:Mn phosphors. *Mater. Chem. Phys.* **2008**, *110*, 43-51. DOI
46. Li, S.; Li, H.; Zhang, H.; Zhang, S.; Lai, Y.; Zhang, Z. Constructing stable surface structures enabling fast charging for Li-rich layered oxide cathodes. *Chem. Eng. J.* **2022**, *427*, 132036. DOI
47. Li, Z.; Li, H.; Cao, S.; et al. Reversible anionic redox and spinel-layered coherent structure enable high-capacity and long-term cycling

of Li-rich cathode. *Chem. Eng. J.* **2023**, *452*, 139041. DOI

48. Cao, J.; Huang, H.; Qu, Y.; Tang, W.; Yang, Z.; Zhang, W. Construction of a hetero-epitaxial nanostructure at the interface of Li-rich cathode materials to boost their rate capability and cycling performances. *Nanoscale* **2021**, *13*, 20488-97. DOI
49. Mohapatra, M.; Seshadri, M.; Naik, Y. P.; Meena, G.; Kadam, R. M.; Singh, V. Radiative properties of 'intense' red emitting $LiAl_5O_8$ :Eu phosphors. *J. Mater. Sci. Mater. Electron.* **2018**, *29*, 7778-84. DOI
50. Yu, H.; Ibrahim, K. B.; Chi, P.; et al. Modulating the voltage decay and cationic redox kinetics of Li-rich cathodes via controlling the local electronic structure. *Adv. Funct. Mater.* **2022**, *32*, 2112394. DOI
51. Xu, G.; Ke, W.; Yu, F.; et al. Modulation of lattice oxygen boosts the electrochemical activity and stability of Co-free Li-rich cathodes. *J. Energy. Chem.* **2022**, *75*, 117-26. DOI
52. Zhang, X.; Belharouak, I.; Li, L.; et al. Structural and electrochemical study of $Al_2O_3$ and $TiO_2$ coated $Li_{1.2}Ni_{0.13}Mn_{0.54}Co_{0.13}O_2$ cathode material using ALD. *Adv. Energy. Mater.* **2013**, *3*, 1299-307. DOI
53. Lu, Q.; Wang, Y.; Yu, K.; Zhao, G.; Cheng, Y.; Yu, Z. One-step constructed oxygen vacancies and Fe-doping to improve the electrochemical performance of Li-rich Mn-based cathode. *J. Alloys. Compd.* **2023**, *937*, 168426. DOI
54. Liu, Y.; Chen, Y.; Wang, J.; et al. Hierarchical yolk-shell structured Li-rich cathode boosting cycling and voltage stabled LIBs. *Nano. Res.* **2022**, *15*, 3178-86. DOI
55. Zhang, P.; Zhai, X.; Huang, H.; et al. Synergistic $Na^+$ and $F^-$ co-doping modification strategy to improve the electrochemical performance of Li-rich $Li_{1.20}Mn_{0.54}Ni_{0.13}Co_{0.13}O_2$ cathode. *Ceram. Int.* **2020**, *46*, 24723-36. DOI
56. Liu, Y.; Yang, Z.; Zhong, J.; et al. Surface-functionalized coating for lithium-rich cathode material to achieve ultra-high rate and excellent cycle performance. *ACS. Nano.* **2019**, *13*, 11891-900. DOI
57. Liu, J.; Wu, Z.; Yu, M.; et al. Building homogenous $Li_2TiO_3$ coating layer on primary particles to stabilize Li-rich Mn-based cathode materials. *Small* **2022**, *18*, e2106337. DOI
58. Zhang, B.; Zhang, Y.; Wang, X.; et al. Role of substitution elements in enhancing the structural stability of Li-rich layered cathodes. *J. Am. Chem. Soc.* **2023**, *145*, 8700-13. DOI
59. Sun, G.; Yu, F.; Zhao, C.; et al. Decoupling the voltage hysteresis of Li-rich cathodes: electrochemical monitoring, modulation anionic redox chemistry and theoretical verifying. *Adv. Funct. Mater.* **2021**, *31*, 2002643. DOI
60. Charbonneau, V.; Lasia, A.; Brisard, G. Impedance studies of $Li^+$ diffusion in nickel manganese cobalt oxide (NMC) during charge/discharge cycles. *J. Electroanal. Chem.* **2020**, *875*, 113944. DOI
61. Zhang, Y.; Shi, X.; Zheng, S.; et al. Alternate heterogeneous superlattice control of lattice strain to stabilize Li-rich cathode. *Energy. Environ. Sci.* **2023**, *16*, 5043-51. DOI